



# Evolution of mesoscale bonded particle clusters in cemented granular material

Zhifu Shen<sup>1</sup> · Feng Gao<sup>1</sup> · Zhihua Wang<sup>1</sup> · Mingjing Jiang<sup>2,3</sup>

Received: 8 December 2017 / Accepted: 11 June 2019 / Published online: 1 July 2019  
© Springer-Verlag GmbH Germany, part of Springer Nature 2019

## Abstract

Research on the macroscopic behavior of cemented granular material in geomechanics is challenged by the lack of understanding in physical origin of experimental observations. Recent advances in microscopic investigations suggest the critical significance of contact behavior, such as bond breakage. The mesoscale link between contact behavior and macroscopic responses has not been well understood so far. Discrete element method (DEM) simulations were carried out in this study to investigate the formation and evolution of bonded particle clusters (i.e., particle groups connected by bonds), which is key mesoscale behavior of cemented granular material. DEM simulation results show that the highly non-uniform deformation within a sample (under imposed uniform strain) leads to spatially non-uniform events of inter-particle bond breakage, which allows the formation of particle clusters. Clusters of various sizes and angularities are interwoven with each other. Under mechanical loading, evolutions of cluster size, number and angularity exhibit three distinctive stages. In stage I (bond breakage ratio  $0 < \omega < 0.3$ ), single particles at spatially random locations are detached from the overall bonded particle skeleton and float in voids of the skeleton. In stage II ( $0.3 < \omega < 0.7$ ), a cluster family with a growing size diversity and continuous size distribution are observed. In stage III ( $0.7 < \omega < 1.0$ ), the maximum cluster size decreases quickly and all bonds are finally broken. Implications of the unique features of cluster evolution for constitutive model development are finally discussed.

**Keywords** Bond breakage · Bonded particle cluster · Cemented granular material · Discrete element method · Mesoscale behavior

## 1 Introduction

Cemented granular materials are common in geotechnical engineering, e.g., structured sands [1, 7, 8, 10], gas hydrate bearing sediments [13, 16, 30, 31, 36] and weak rocks [6, 27, 28]. Their macroscopic mechanical behavior has been extensively studied experimentally. There are mainly three categories of constitutive models developed to describe their behavior following different constitutive

model frameworks. (1) Modified elasto-plastic constitutive models developed from the remolded soils' model. These modified models treat cemented granular material as a continuous single-phase material [34]. (2) Binary-mixture-type models where cemented granular material is treated as a composite material consisting of two parts, i.e., structured part and remolded part [12, 14, 47]. (3) Micromechanics-based model that derives the macroscopic behavior of cemented granular material from the collection of contact behavior [15]. These models can capture the general behavior of cemented granular material, but further improvement is required for model capability. However, there is no real progress in these models in the last decade mainly due to, in the authors' opinion, a lack of understanding in how damage develops inside a sample.

The binary-mixture-type models seem closer to the physical scenario of damage development in cemented granular material than it being treated as a single-phase

✉ Zhihua Wang  
wzhnjut@163.com

<sup>1</sup> Institute of Geotechnical Engineering, Nanjing Tech University, Nanjing 210009, China

<sup>2</sup> Department of Geotechnical Engineering, College of Civil Engineering, Tongji University, Shanghai 200092, China

<sup>3</sup> Department of Civil Engineering, Tianjin University, Tianjin, China

material. The two parts (structured part and remolded part) in a binary-mixture-type model may be defined in terms of physical entity, e.g., uncemented granular assembly plus cement agent material [14] as shown in Fig. 1a. Alternatively, the two parts can be defined as two sources of shear strength [47] as shown in Fig. 1b or as two reference states [12] as depicted in Fig. 1c. In a general binary-mixture-type model framework, the stresses  $\sigma_{ij}$  and strain increments  $d\varepsilon_{ij}$  for each part are assembled to obtain the overall constitutive behavior:

$$\sigma_{ij} = (1 - D_\sigma)\sigma_{ij}^s + D_\sigma\sigma_{ij}^r, \quad d\varepsilon_{ij} = (1 - D_\varepsilon)d\varepsilon_{ij}^s + D_\varepsilon d\varepsilon_{ij}^r \quad (1a, b)$$

$$d\sigma_{ij}^s = D_{ijkl}^s d\varepsilon_{kl}^s, \quad d\sigma_{ij}^r = D_{ijkl}^r d\varepsilon_{kl}^r \quad (2a, b)$$

where  $D_\sigma$  and  $D_\varepsilon$  are two weighting variables, the superscripts ‘s’ and ‘r’ represent structured part and remolded part, respectively, and  $D_{ijkl}$  is the constitutive matrix.

The binary-mixture-type models try to respect the granular nature of the material. However, due to the extreme lack of understanding of material behavior at subsample scales (e.g., micro-/particle scale and meso-/particle-group scale), the highly conceptualized models in Fig. 1 and Eqs. (1–2) often cannot satisfactorily reproduce soil behavior in a unified way. A physically meaningful way to partition the two parts has not been proposed, either. Difficulty arises when distributing stresses and strains between the two parts in Eq. (1); it is usually simply assumed that the two parts share the same strain, which is often improper. To fulfill the potential of the physically elegant binary-mixture-type models, it is necessary to investigate the subsample scale behavior of cemented granular material, which is also valuable for the development of micromechanics-based model.

Advanced microscopic experimental techniques have been widely applied to study the responsible microstructures behind the observed macroscopic behavior [6, 9, 16, 17], which facilitates the application of advanced numerical tools, such as discrete element method (DEM), to bridge the scales. In DEM, cemented granular material is regarded as an assembly of particles bonded at contacts. The bond contact behavior has been studied experimentally [11, 21, 22, 25], numerically [39] and analytically [44]. Bond contact models were developed and implemented in DEM [4, 5, 19, 20, 24, 35, 37, 38, 40, 41], including consideration of particle crushing [3]. Particle cluster presence has been reported in experiments [29] and DEM simulations [40, 42, 43]: Bonded particle clusters are *naturally* formed and subsequently crushed as a result of inter-particle bond breakage, which will be further analyzed in this study. As a significant mesoscale behavior, the evolution of these clusters fundamentally determines the macroscopic behavior which is critically important for constitutive model development. For example, in micromechanics-based model framework, the presence of clusters in cemented granular material requires a granular hexagon description of the mesoscale geometrical and kinematical behavior, such as the H-microdirectional model for clean granular material [32, 33].

Despite these qualitative advancements, quantitative description of particle cluster evolution has not been reported before, which constitutes the motivation of this study. Nondestructive and continuous acquisition of particle cluster configuration is almost impossible with current experimental techniques. With the aid of DEM simulations, this study tracks the evolution of particle clusters in numerical cemented granular materials following various loading paths. Information such as cluster size, shape,

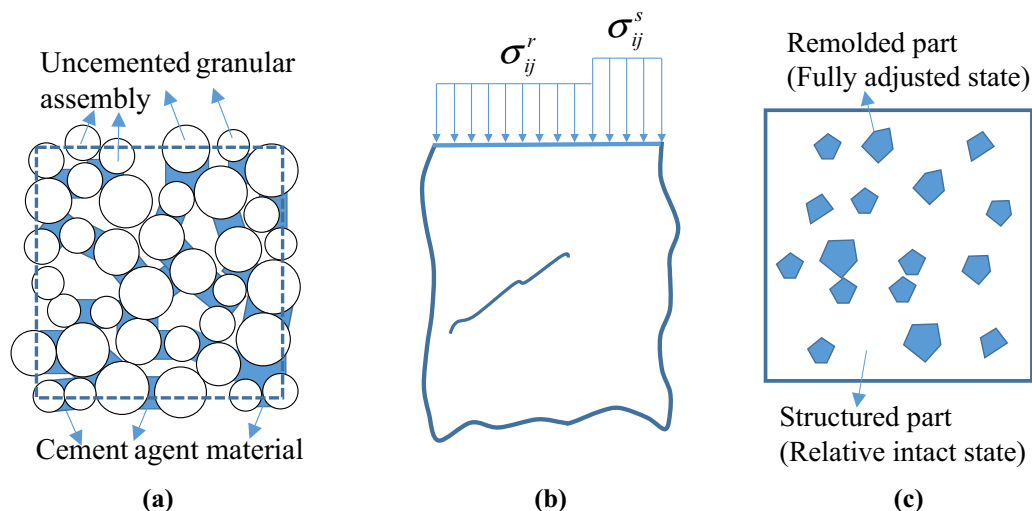


**Fig. 1** Conceptualized material components in the binary-mixture-type models: **a** uncemented granular assembly plus cement agent material [14], **b** two sources of shear strength [47] and **c** two reference states [12]

position and number is analyzed. The implication of the results for constitutive model development is discussed.

## 2 Bond contact model and DEM simulations

Structured sand, as a typical cemented granular material, was modeled in this study by applying the bond contact model developed in [40], which has been implemented in PFC3D by the authors [18]. The salient features of this bond contact model are recalled below.

Cemented granular material was idealized as an assembly of bonded spheres. Since grains are simplified as spheres, the bond material between two spheres (with an average diameter of  $D_s$ ) can be idealized in shape as a short cylinder (referred to as bond cylinder hereafter) with a diameter of  $D_b$  and a length of  $H_b$ , as shown in Fig. 2. The bond cylinder connects two particles' surfaces and thus has two spherical concave ends. This bond shape is much closer to reality than previous models that assume beam connection of two bonded particles. Two types of bond contacts (*thin bond* and *thick bond*) are considered. In a thin bond contact, the bond material deposits at a physical contact (two particles being in contact); in a thick bond contact, the bond material deposits at a virtual contact (two particles being close but not in contact). It is assumed that the bond agent material is sparsely distributed in space at either a thin or a thick contact and there is no interaction between bond materials from any two bond contacts. This assumption best applies to the microscopic structure of low bond content cases in structured sand [40], gas hydrate bearing sediment [38] and some weak rocks [24].

The bond contact model used in this study incorporates complete interactions of two particles in the normal, tangential, rolling and torsion directions. Thus, the bond failure criteria include five basic failure modes (compression, tension, shear, rolling and torsion) and a coupled shear–rolling–torsion failure mode, as shown in Fig. 3.

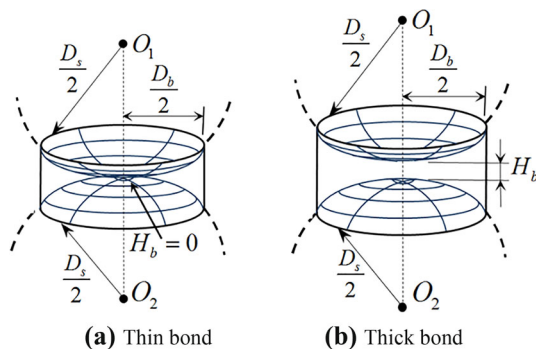


Fig. 2 Two types of bond contacts modeled

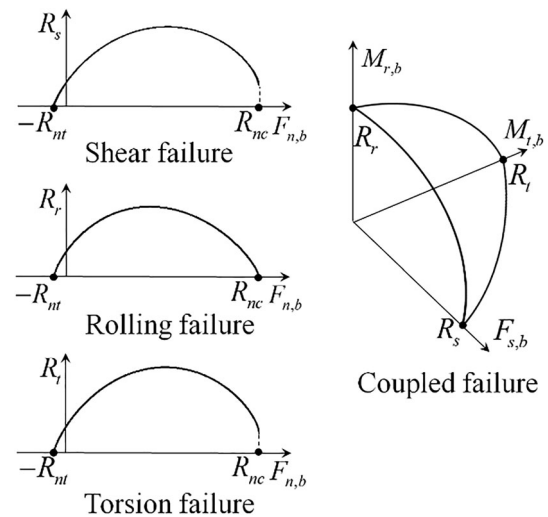


Fig. 3 Bond failure criterion

In pure compression failure, a bond is crushed by a compressive force that exceeds the ultimate compressive strength  $R_{nc}$ . In pure tension failure, a bond is pulled apart by a tensile force that exceeds the ultimate tensile strength  $R_{nt}$ . Based on study in [39], we have

$$R_{nc} = \chi_c \sigma_c \pi (D_b/2)^2, \quad R_{nt} = \chi_t \sigma_t \pi (D_b/2)^2 \quad (3a, b)$$

where  $\sigma_c$  and  $\sigma_t$  are the compressive and tensile strengths of the bond material. The two factors  $\chi_c$  and  $\chi_t$  account for the bond geometry effect on bond strength. According to [39],  $\chi_c$  and  $\chi_t$  can be correlated to two dimensionless geometry factors of the bond cylinder,  $m = H_b/D_b$  and  $n = D_s/D_b$ , as

$$\chi_c = C_1 e^{C_2 m} n^{C_3}, \quad \chi_t = 1 \quad (4a, b)$$

where  $C_1$ ,  $C_2$  and  $C_3$  are three fitting parameters.

Apart from pure compressive and tensile failure modes, a bond may fail in shear, rolling or torsion mode under a bond normal force  $F_{n,b}$  with  $-R_{nt} < F_{n,b} < R_{nc}$ . The corresponding strength  $R_i$  ( $i = s$  in shear failure,  $i = r$  in rolling failure and  $i = t$  in torsion failure) depends on the compression strength  $R_{nc}$ , the tension strength  $R_{nt}$  and the bond diameter  $D_b$ ,

$$R_s = S_s (R_{nc} + R_{nt}) \quad (5)$$

$$R_r = S_r (R_{nc} + R_{nt}) D_b/2 \quad (6)$$

$$R_t = S_t (R_{nc} + R_{nt}) D_b/2 \quad (7)$$

The parameter  $S_i$  is a quantity capturing the effect of normal force on strength,

$$S_i = m_{i1} f_n + m_{i2} f_n [\ln(f_n^{-1})]^{m_{i3}} \quad (8)$$

where  $m_{i1}$ ,  $m_{i2}$ ,  $m_{i3}$  ( $i = s, r, t$ ) are fitting parameters and  $f_n$  is a normalized bond normal force that can be expressed as

$$f_n = (F_{n,b} + R_{nt}) / (R_{nc} + R_{nt}) \quad (9)$$

The strength envelopes are shown in Fig. 3.

Note that Eqs. (5–7) give the bond strength when only shear or rolling or torsional load is acting on the bond cylinder in addition to the normal force. In a general case, the shear force  $F_{s,b}$ , rolling moment  $M_{r,b}$  and torque  $M_{t,b}$  together bring a bond to breakage in a coupled way. A coupled failure criterion can be practically described by

$$f_s^2 + f_r^2 + f_t^2 \begin{cases} < 1 & \text{intact} \\ \geq 1 & \text{broken} \end{cases} \quad (10)$$

where the normalized loads are  $f_s = F_{s,b}/R_s$ ,  $f_r = M_{r,b}/R_r$ , and  $f_t = M_{t,b}/R_t$ . This coupled failure criterion is visualized in Fig. 3.

It should be noted that the bond geometry effects described in Eq. (4) and the failure criteria in shear, rolling and torsion described in Eqs. (5–10) have been proposed based on experiments on glued aluminum rod/sphere pairs [21, 22] and numerical simulations [39]. The parallel bond model in PFC [18] can be used as well if a simple model is desired.

For bond installation, only bond cylinder with a slenderness ratio  $H_b/D_b$  less than a threshold ( $m_0$ ) is allowed to be implemented. A slim bond is not allowed since it is rarely observed in real cemented granular material and it is also mechanically fragile, thus contributing little to the macroscopic strength. The threshold  $m_0$  is assumed the same for different bond contents.  $D_b$  is assumed to follow a normal distribution. For DEM sample with a higher bond content, the bond cylinder diameter  $D_b$  is greater, and thus,  $H_b$  is greater, allowing particles with a larger distance to be bonded. Therefore, higher bond content means more bonded contact and greater bond cylinder size at each contact, leading to a greater bond strength according to Eqs. (5–7). This bond installation methodology is qualitatively based on SEM observations of structured sands [6, 9, 16, 17].

The contact after bond breakage behaves in an unbonded way as described by [23]. The contact behavior after bond breakage is described by a 3D unbonded contact model with rolling and twisting resistances [23]. For a thick bond, after bond breaks, the bond material can bridge the gap between the two previously cemented particles so that the two particles can interact as if they were enlarged in size. This is captured in the model by modifying the contact detection threshold so that the two previously bonded particles can interact even if there is a gap between them. This modification is not implemented for a thin bond. For a post-breakage unbonded contact, the attached bond material on grain surface can increase particle angularity and this is captured in the model by increasing the peak rolling and twisting resistances. The above two modifications in unbonded contact behavior are not implemented for a

newly created unbonded contact. See details of the post-breakage unbonded contact in [40]. Capturing such transition has only a very small effect on the quasi-static simulations in this paper. But the authors believe that it would be important for dynamic problem.

The failure of a bonded contact is brittle and can be accompanied by plastic-like sliding/rolling/twisting, contact splitting (in purely tensile failure) or bond crushing (in purely compressive failure) and local adjustment of structure. In our simulations with a low loading rate (axial strain rate = 1%/min), local damping in PFC3D [18] with a damping coefficient of 0.7 was used. The energy release event due to bond breakage was temporally and spatially sparse. Since the bonding effects are weak, the released energy was timely damped so that the overall damage process evolved in a smooth way, unlike concentrated energy release in events like rock burst. Changing the damping coefficient to a lower value (0.4) would only slightly change the numerical results (less than 2% in the stress–strain curve). The very little effect of damping is a result of the very slow loading.

The model parameters are listed in Table 1. See details about their physical meanings and a parametric study in [40]. It is emphasized that this study is based on the widely

**Table 1** Contact model parameters

Parameter	Value	
Unbonded contact	Equivalent contact modulus, $E_p$	0.7 GPa
	Ratio of normal stiffness to tangential stiffness, $\xi$	5
	Inter-particle friction coefficient, $\mu$	0.5
	Particle shape parameter used to consider the mechanical effects of particle angularity, $\beta_c$	0.15
	Local crushing parameter, $\zeta_c$	4
	Bonding material	Ratio of bond modulus $E_b$ to equivalent contact modulus $E_p$ , $E_b/E_p$
Poisson's ratio, $\nu_b$		0.2
Compressive strength, $\sigma_c$		80 MPa
Tensile strength, $\sigma_t$		7 MPa
Threshold of bond slenderness ratio, $m_0$		0.1
Bond distribution parameter, $w$		0.2
Bond failure criterion (fitting parameters)		Compressive failure: $C_1 = 1.444$ , $C_2 = -0.702$ , $C_3 = 0.168$
	Tangential failure: $m_{s1} = 0.055$ , $m_{s2} = 0.439$ , $m_{s3} = 0.696$	
	Rolling failure: $m_{r1} = 0.0$ , $m_{r2} = 0.324$ , $m_{r3} = 0.757$	
	Torsional failure: $m_{t1} = 0.031$ , $m_{t2} = 0.327$ , and $m_{t3} = 0.692$	

accepted notion that realistic structured sand and the idealized “DEM material” share common bond effects and granular nature. Therefore, it is practical to choose parameters within common ranges, instead of against a specific structured sand.

Cubic samples with  $N_p = 40,000$  spherical particles were simulated in this study. The particle size distribution is shown in Fig. 4. Samples were generated by radius expansion method in a box of six rigid frictionless walls to achieve a uniform and isotropic microstructure. An isotropic stress state of 50 kPa was reached before the bond contact model installation. Four samples were modeled to study the effects of sample density (void ratio  $e_0$ ) and bond content (denoted by  $c$ , the ratio of all bond material volume over all particle volume): S1 ( $e_0 = 0.80$ ,  $c = 1.0\%$ ), S2 ( $e_0 = 0.80$ ,  $c = 3.0\%$ ), S3 ( $e_0 = 0.92$ ,  $c = 1.0\%$ ) and S4 ( $e_0 = 0.92$ ,  $c = 3.0\%$ ).

Note that the bonds do not take any load when it is first installed under the isotropic stress of 50 kPa. This corresponds to the formation of bonding materials possibly through a depositional process after the ground soil skeleton has reached a stable state. Subsequent numerical tests try to mimic geotechnical engineering activities following some simple, idealized loading paths. Complex stress and initial bond conditions reproducing reality can be implemented as well, although the simplest conditions were simulated here.

The boundary walls were rigid and frictionless throughout the sample generation and subsequent loading stages. It has been checked that the samples showed a spatial void ratio fluctuation within 10%, which was assessed by measuring local void ratios across a sample. Judging from the particle cluster configuration to be discussed below, there is no tendency of less or more bond breakage near the boundary. Therefore, the boundary effects are negligible.

The test conditions are shown in Table 2. All the four samples were tested under true triaxial compression (TTC) conditions with a mean stress  $p = 400$  kPa and an intermediate principal stress ratio  $b = (\sigma_2 - \sigma_3)/(\sigma_1 - \sigma_3) = 0.0$ , i.e.,  $\sigma_2 = \sigma_3$ . Besides, TTC tests on S1 were also

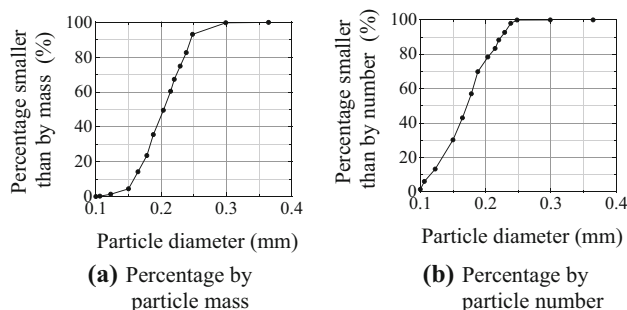


Fig. 4 Particle size distribution

Table 2 Numerical samples and test conditions in DEM simulations

Sample	S1	S2	S3	S4
Bond content	1%	3%	1%	3%
Initial void ratio	0.80	0.80	0.92	0.92
Thin bond percent by no.	44.1%	41.4%	49.7%	46.6%
Tests	TTC ( $b = 0.0-1.0$ ), CTC	TTC ( $b = 0.0$ )	TTC ( $b = 0.0$ )	TTC ( $b = 0.0$ )

TTC: True triaxial compression, CTC: conventional triaxial compression

simulated to investigate the effects of the intermediate principal stress ratio value ( $b$ ). Conventional triaxial compression (CTC) tests on S1 under four different confining pressures (100–800 kPa) were simulated to study the effects of stress level.

### 3 Macroscopic behavior

Figure 5 presents the macroscopic behavior of the simulated structured sands. Figure 5a shows that increased stress level (confining pressure  $\sigma_3$ ) can reduce the peak deviator stress ratio  $\eta (= q/p)$  and suppress the volumetric dilation (decrease of void ratio  $e$ ). Figure 5b shows that an increase in  $b$ -value leads to a decrease in peak strength but an increase in dilation. Under non-axisymmetric stress conditions ( $b = 0.25, 0.5, 0.75$ ), the rapid softening is a result of persistent strain localization, which leads to the premature plateau in void ratio. Figure 5c shows that increase in sample density (decrease in void ratio) and bond content can increase the peak strength and dilation. The softening behavior of sample S3 is accompanied with contraction in Fig. 5c, which is a feature of loose weakly cemented soil. Note that the observed steady void ratio for samples S2 sand S4 in Fig. 5c is transient. Further loading will lead to its decrease to the steady-state void ratio of clean sand. Our DEM simulations covered a wide range of sample density and bond content and replicated typical behavior of structured sand. Therefore, the following discussions on bond breakage and particle clusters should be widely representative. Note that under axisymmetric stress condition, the rigid wall is successful to impose overall uniform deformation, thus facilitating the study of particle cluster evolutions.

Bond breakage ratio  $\omega$  is defined as the ratio of broken bond number over total initial bond number. Figure 6



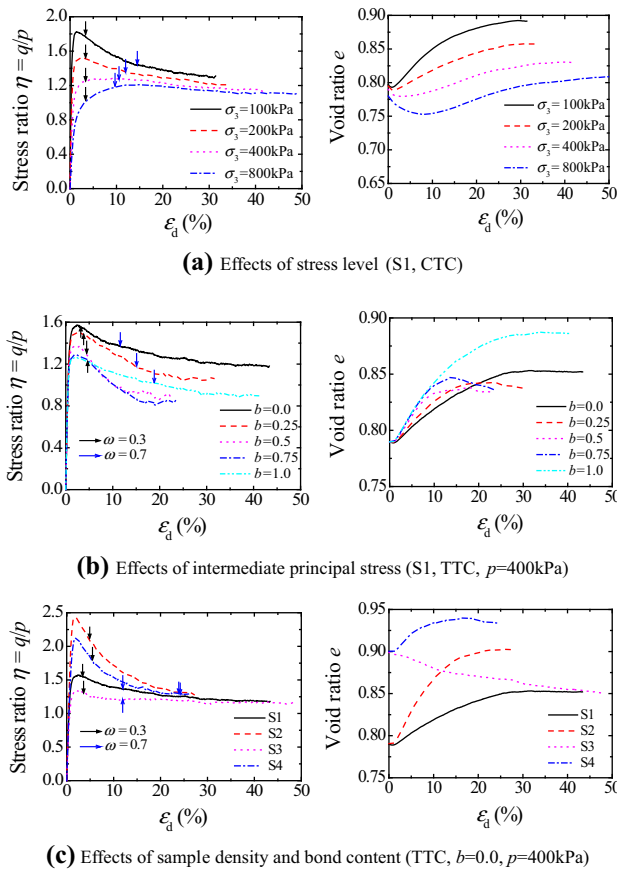


Fig. 5 Macroscopic behavior of simulated structured sands

presents the evolutions of  $\omega$  in all the simulated samples. The increase in stress level and decrease in  $b$ -value can increase the bond breakage ratio at the same deviator strain. Bond breaks more rapidly in samples with lower bond content, and sample density only slightly affects the bond breakage rate. Strain localization slows down the overall bond breakage rate because breakage concentrates in the shear band.

### 4 Mesoscale deformation and cluster formation mechanism

Due to the heterogeneous nature of granular material, the macroscopic uniform deformation never means uniform deformation at mesoscale. The local incremental displacement gradient  $dH^{loc}$  introduced in [2] was used to evaluate the displacement gradient response in a void cell so that structured deformation pattern at mesoscale (including transient and developing persistent strain localizations) can be visualized. Each void cell was a tetrahedron constructed using the Delaunay tessellation method. The four vertices of a tetrahedron are particles whose incremental displacements were used to calculate

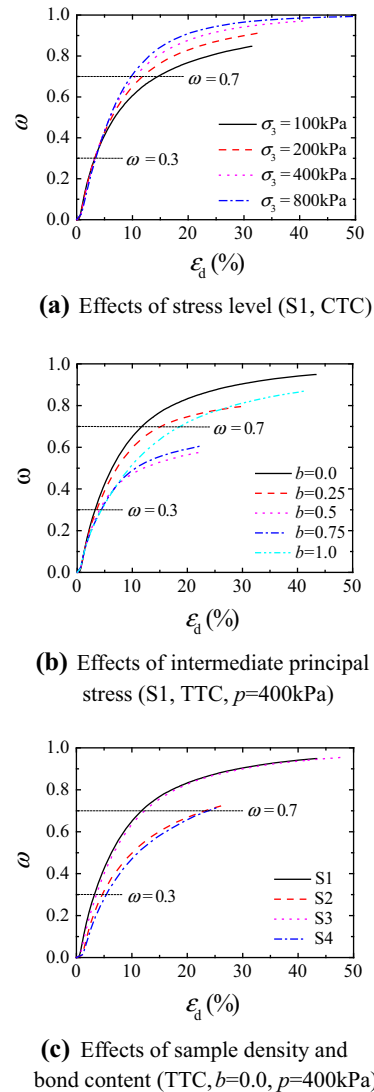


Fig. 6 Evolutions of bond breakage ratio  $\omega$

each  $dH^{loc}$ . To view the spatial distribution of  $dH^{loc}$  in an assembly, a dimensionless quotient  $e^{loc}$  defined in [26] was calculated for each tetrahedron:

$$e^{loc} = \frac{dH_{ij}^{loc} d\varepsilon_{ij}^{avr}}{d\varepsilon_{ij}^{avr} d\varepsilon_{ij}^{avr}} \tag{11}$$

where  $d\varepsilon^{avr}$  is the uniform incremental displacement gradient imposed on the boundary walls.

The deviation magnitude of  $e^{loc}$  from unit describes the degree of deviation of void cell incremental displacement gradient from the average. Figure 7 presents the spatial distributions of  $e^{loc}$  calculated within an incremental axial strain of  $d\varepsilon_a = 0.06\%$ . For  $b = 0.0$  case in Fig. 7a–c, the incremental displacement gradient is not uniform but concentrates into some seemingly random regions/microbands; such localization is transient, and therefore, no shear band is recognized even when  $\varepsilon_d$  reaches 41.5%. For

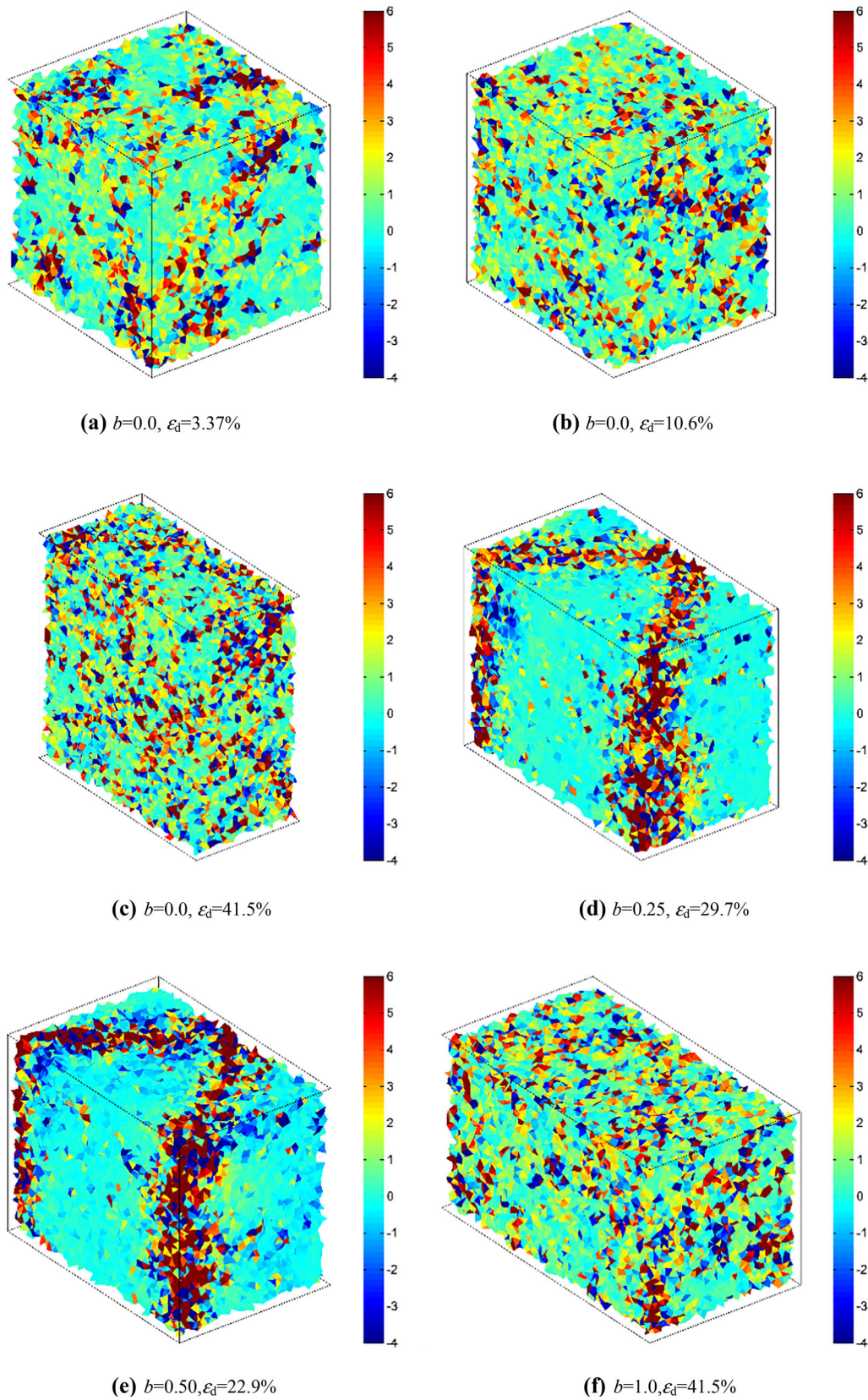
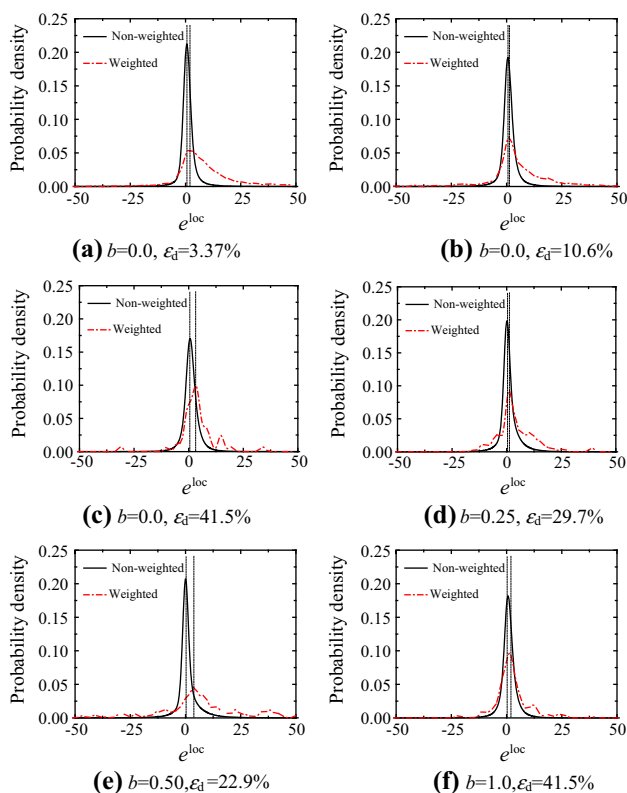


Fig. 7 Spatial distributions of dimensionless quotient  $e^{loc}$  at different deviator strains (S1, TTC,  $p = 400$  kPa)

$b = 0.25$  case, the incremental displacement gradient is localized into two distinctive shear bands with a width of about 10 tetrahedral cells. The deformation patterns in Fig. 7 are typical for axisymmetric and non-axisymmetric loading conditions.

To explore the link between local displacement and bond breakage, two datasets are prepared: (1) non-weighted set including  $e^{\text{loc}}$  of all tetrahedron cells, and (2) weighted set including  $e^{\text{loc}}$  of all tetrahedron cells but  $e^{\text{loc}}$  of each cell is counted  $n$  times where  $n (\geq 0)$  is the number of edges that experience bond breakage in a cell during an incremental deformation. The authors think that the  $n$ -value can represent the degree of involvement of a cell in bond breakage and particle cluster formation. Therefore, the weighted dataset can be a proper quantitative descriptor of mesoscale behavior of cemented granular material. Figure 8 presents the probability densities of both datasets. In Fig. 8, the non-weighted set exhibits a symmetric distribution about  $e^{\text{loc}} = 1$ . The weighting manipulation leads to a rightward (positive) shift of the peak density position. The area under the shifted curve is greater on the  $e^{\text{loc}} > 1$  side than on the  $e^{\text{loc}} < 1$  side. Therefore, the large cell-level deformation rate is a consequence of bond breakage. The spatially non-uniform distribution of  $e^{\text{loc}}$  indicates non-uniform bond breakage across the sample. The



**Fig. 8** Probability densities of  $e^{\text{loc}}$  in non-weighted and weighted datasets

presence of clusters was confirmed in experiments, where structured sands were immersed in deaired water after triaxial compression tests and were found to form a “cohesionless heap” with grain clusters and blocks [29].

Initially (before deviator loading), all particles are bonded and the whole sample can be viewed as one cluster. Figure 9 presents a typical spatial configuration of particle clusters when the deviator strain reaches 14.3%. Particle clusters were identified by particle labeling method. In this method, all particles are first labeled with number ‘0.’ A traversal of all particles is executed to modify the labels so that particles with the same label belong to the same cluster. For each traversed particle  $P_i$  in an outer loop, all particles connected with  $P_i$  through bond contacts are traversed in an inner loop. The labels of  $P_i$  and its bonded neighbors are sorted from the minimum  $L_{\min}$  to  $L_{\max}$  and denote  $L_{\min+1}$  the second minimum of their label numbers.

1. If  $L_{\min} = L_{\max} = 0$ ,  $P_i$  and its bonded neighbors have not been assigned to a cluster before, and therefore, they are labeled with a number  $Q_c$ . Then,  $Q_c$  is updated to  $Q_c + 1$ . Initially,  $Q_c$  equals to 1.
2. If  $L_{\min} = L_{\max} \neq 0$ ,  $P_i$  and its bonded neighbors have already been assigned to the same cluster, and therefore, their labels will not be modified.
3. If  $0 < L_{\min} < L_{\max}$ ,  $P_i$  and its bonded neighbors are assigned to different clusters, but they should belong to the same cluster. Therefore, particles in the sample with a label between  $[L_{\min}, L_{\max}]$  are re-labeled with  $L_{\min}$ .
4. If  $0 = L_{\min} < L_{\max}$ , some particles among  $P_i$  and its bonded neighbors have already been assigned to one or more clusters while the rests have not. Therefore, particles in the sample with a label between  $[L_{\min+1}, L_{\max}]$  are re-labeled with  $L_{\min+1}$ . Particles among  $P_i$  and its bonded neighbors with a label of ‘0’ are also assigned with a label of  $L_{\min+1}$ .

The above procedures are repeated for each traversed particle  $P_i$ . Finally, the clusters are distinguished by colors according to their number label.

In Fig. 9, there are totally 17, 966 clusters, including single-particle clusters. Clusters are grouped by their sizes, denoted by  $D_{\text{clt}}$  (the number of member particles in a cluster). The number of clusters in a size group is denoted by  $N_{\text{clt}}$ . In each view of Fig. 9, one or more groups of clusters are shown while other groups are set transparent for nice visualization. Note that clusters are generally randomly distributed in the sample domain, resulting from the overall uniform deformation under axisymmetric loading. Under non-axisymmetric loading, for example  $b = 0.25$  in TTC test as shown in Fig. 10, the largest three wedge-shaped clusters span across the sample and they are separated by two shear bands. Bond breakage mainly



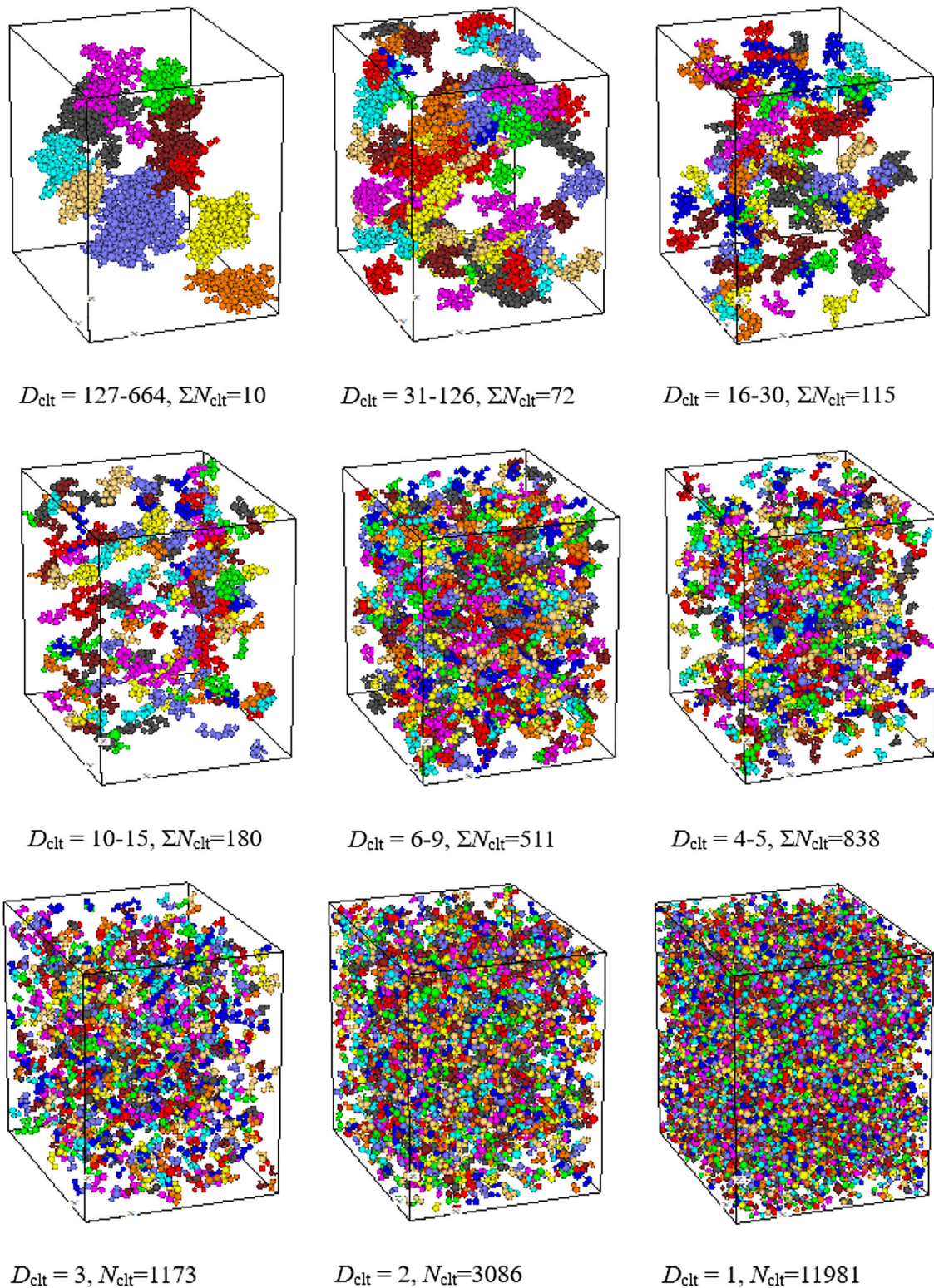


**Fig. 9** Spatial configuration of bonded particle clusters (sample S1, TTC,  $b = 0.0$ ,  $p = 400$  kPa, deviator strain  $\varepsilon_d = 14.3\%$ , bond breakage  $\omega = 75.5\%$ )

occurs within the shear band while bond breakage percent outside the shear band is very small. The focus of this study is put on the uniform deformation conditions.

Figure 9 shows that clusters are featured by highly angular shapes and the angularity tends to decrease as clusters become small in size. To quantitatively investigate

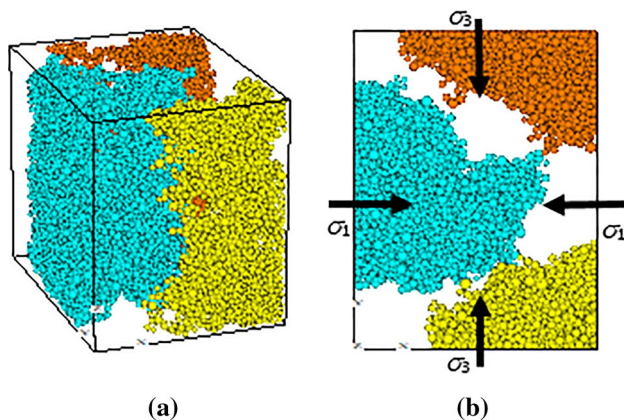


**Fig. 10** Spatial configuration of particle clusters under non-axisymmetric loading (sample S1, TTC,  $b = 0.25$ , deviator strain  $\epsilon_d = 16.3\%$ , bond breakage  $\omega = 71.3\%$ ): **a** perspective view and **b** plane view (major–minor principal stress plane). Only the largest three clusters are shown

the evolution of cluster features, cluster angularity and integrity indices are introduced. Cluster angularity is defined as  $\rho = d_{\max}/(2R_{\text{eq}}) - 1$ , where  $d_{\max}$  is the maximum dimension of a cluster, obtained by searching the maximum value of the distance between any two member particles' centroids in a cluster plus the sum of their radii.  $R_{\text{eq}}$  is the equivalent radius of the cluster defined as

$$R_{\text{eq}} = \left( \frac{3}{4\pi} \sum_{i=1}^{D_{\text{clt}}} V_i \right)^{1/3} \tag{12}$$

where  $V_i$  is the volume of the  $i$ th member particle in a cluster.

By definition,  $\rho$  equals to 0 for sphere. Although particles in a cluster are connected through bonds, there can be unbonded contacts between them as well, which act as weak points inside a cluster. Cluster integrity index  $I$  is thus defined as the ratio of bond contact number over total contact number in a cluster. Figure 11 presents typical relationships between cluster size and volume-weighted average angularity and integrity ( $\rho_{\text{avr}}$  and  $I_{\text{avr}}$ ) of clusters in a size group, which are defined as

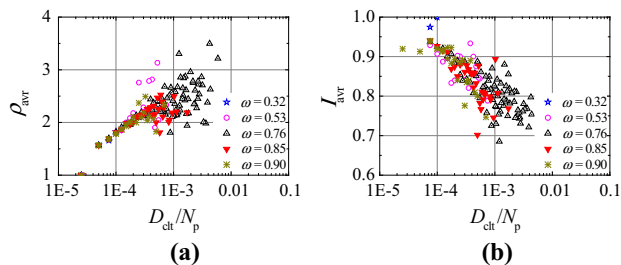


**Fig. 11** Relationships between **a** average cluster angularity  $\rho_{\text{avr}}$  and normalized cluster size  $D_{\text{clt}}/N_p$ , and **b** average cluster integrity  $I_{\text{avr}}$  and normalized cluster size  $D_{\text{clt}}/N_p$  (sample S1, TTC,  $b = 0.0$ ,  $p = 400$  kPa)

$$\rho_{\text{avr}} = \frac{\sum_{i=1}^{n_g} \rho_i V_i}{\sum_{i=1}^{n_g} V_i}, \quad I_{\text{avr}} = \frac{\sum_{i=1}^{n_g} I_i V_i}{\sum_{i=1}^{n_g} V_i} \tag{13a, b}$$

where  $\rho_i$  and  $I_i$ , respectively, are angularity and integrity, respectively, of cluster  $i$  with a volume of  $V_i$  and  $n_g$  is the number of clusters in the size group.

Figure 9 only provides a snapshot in the whole loading process while Fig. 11 offers an evolving view at various values of  $\omega$  from 0.039 to 94.5%. Figure 11 shows that smaller clusters have lower angularity and greater integrity compared with larger clusters.

### 5 Cluster evolution

To examine the dynamic process of cluster formation and crushing, Fig. 12 presents the evolutions of cluster number, size and angularity throughout the loading process. As a result of the successive crushing of larger clusters into smaller ones, in Fig. 12a, the total cluster number ( $N_{\text{tot}}$ ) increases with bond breakage ratio  $\omega$  at a constant rate in the range of (0, 0.3) and (0.7, 1.0) and the rate keeps increasing in the range of (0.3, 0.7). Similar variation is observed for single-particle cluster number ( $N_{\text{sgl}}$ ) in Fig. 12b. In Fig. 12c, the maximum cluster size ( $D_{\text{clt,max}}$ ) decreases with  $\omega$  in a sigmoidal pattern:  $D_{\text{clt,max}}$  first decreases slowly when  $\omega$  is less than 0.3, followed by a sharp drop before  $\omega$  exceeds 0.7, and then, again  $D_{\text{clt,max}}$  decreases at a very low rate. In Fig. 12d, the volume-weighted average cluster angularity of all clusters ( $\rho_{\text{avr}}^*$ ) shows a unimodal variation pattern with  $\omega$  and reaches a peak at  $\omega = 0.7$ . When  $\omega$  is less than 0.3,  $\rho_{\text{avr}}^*$  changes only slightly. In Fig. 12, all the simulated samples exhibit almost the same evolution process except for under non-axisymmetric loading conditions where localization occurs.

In Fig. 9, with reduction in cluster size, the number of clusters in that size group increases significantly. A plot of ( $D_{\text{clt}}, N_{\text{clt}}$ ) would give a complete view of the cluster family, similar to the function of particle size distribution curve. In Fig. 13a,  $D_{\text{clt}}$  is normalized by  $N_p$  and  $N_{\text{clt}}$  is normalized by  $N_{\text{sgl}}$ . Figure 13a shows that in a double-logarithmic plot, cluster number decreases linearly with the increase in cluster size; this trend can be fitted by a linear function (see the lines for  $\omega = 0.31$  and  $0.76$  in Fig. 13a as examples). The fitted lines are forced to pass a specific point ( $2.5e - 5, 1$ ) that represents single-particle cluster, i.e.,  $D_{\text{clt}}/N_p = 1/40,000$ ,  $N_{\text{clt}}/N_{\text{sgl}} = 1$ . Note that in Fig. 12b the way  $N_{\text{sgl}}$  increases with  $\omega$  is unique, independent of all factors examined in this study. Therefore,  $N_{\text{sgl}}$  acts as a

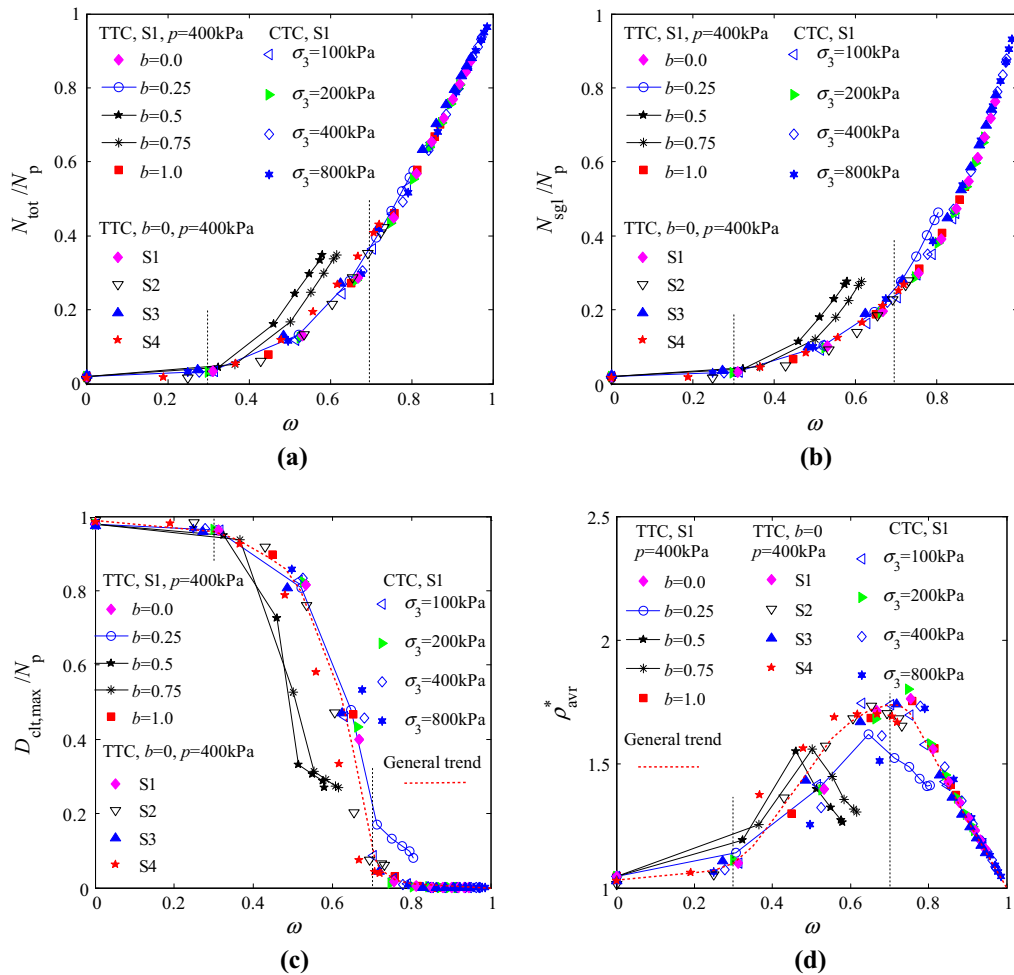


Fig. 12 Evolutions of **a** total cluster number, **b** single-particle cluster number, **c** maximum cluster size and **d** cluster angularity

perfect reference point for the fitting purpose in Fig. 13a. The fitting relationship between  $D_{clt}$  and  $N_{clt}$  is

$$\log\left(\frac{N_{clt}}{N_{sgl}}\right) = A \left[ \log\left(\frac{D_{clt}}{N_p}\right) - \log\left(\frac{1}{N_p}\right) \right] \quad (14)$$

where  $N_p = 40,000$  is constant in this study while  $N_{sgl}$  is a function of  $\omega$  as shown in Fig. 12b.

In Eq. (14), parameter  $A$  is determined by curve fitting. Figure 13b shows that  $A$  is a unimodal function of  $\omega$ , slightly influenced by sample void ratio, bond content, stress level and loading path. The general trend (dash curve in Fig. 13b) presents an initial increase in  $A$  with  $\omega$ , reaching the maximum of  $-2.3$  at  $\omega = 0.7$ , and then,  $A$  decreases rapidly toward the theoretical negative infinite. For non-axisymmetric loading cases (TTC tests,  $b = 0.25, 0.50, 0.75$ ), a premature decrease in  $A$  is observed (the ‘line + symbol’ data in Fig. 13b).

The value of  $D_{clt}$  when  $N_{clt} = 1$  (denoted by  $D_{clt}^*$ ) is of special interest because it represents a threshold size of

cluster below which the quantity of clusters can be well described in a statistic way by Eq. (14). Clusters larger than  $D_{clt}^*$  are so sparsely distributed along  $D_{clt}$  axis and are so small in quantity that they can hardly be described statistically. Hereafter, clusters larger than  $D_{clt}^*$  are named *disperse clusters*, while clusters smaller than  $D_{clt}^*$  are named *effective clusters*. The spatial configuration of clusters in Fig. 9 can be viewed as *disperse clusters* embedded in the matrix of *effective clusters*. From the fitted parameter  $A$ ,  $D_{clt}^*$  can be back-calculated and shows a unimodal variation pattern with  $\omega$  in Fig. 13c.

Figures 12 and 13 show that the quantities describing cluster evolution process are similar among samples of different void ratios and bond contents and under different loading conditions. This implies the existence of a general law governing the cluster evolution and the potential application of the observed mesoscale behavior to constitutive model development is discussed below.



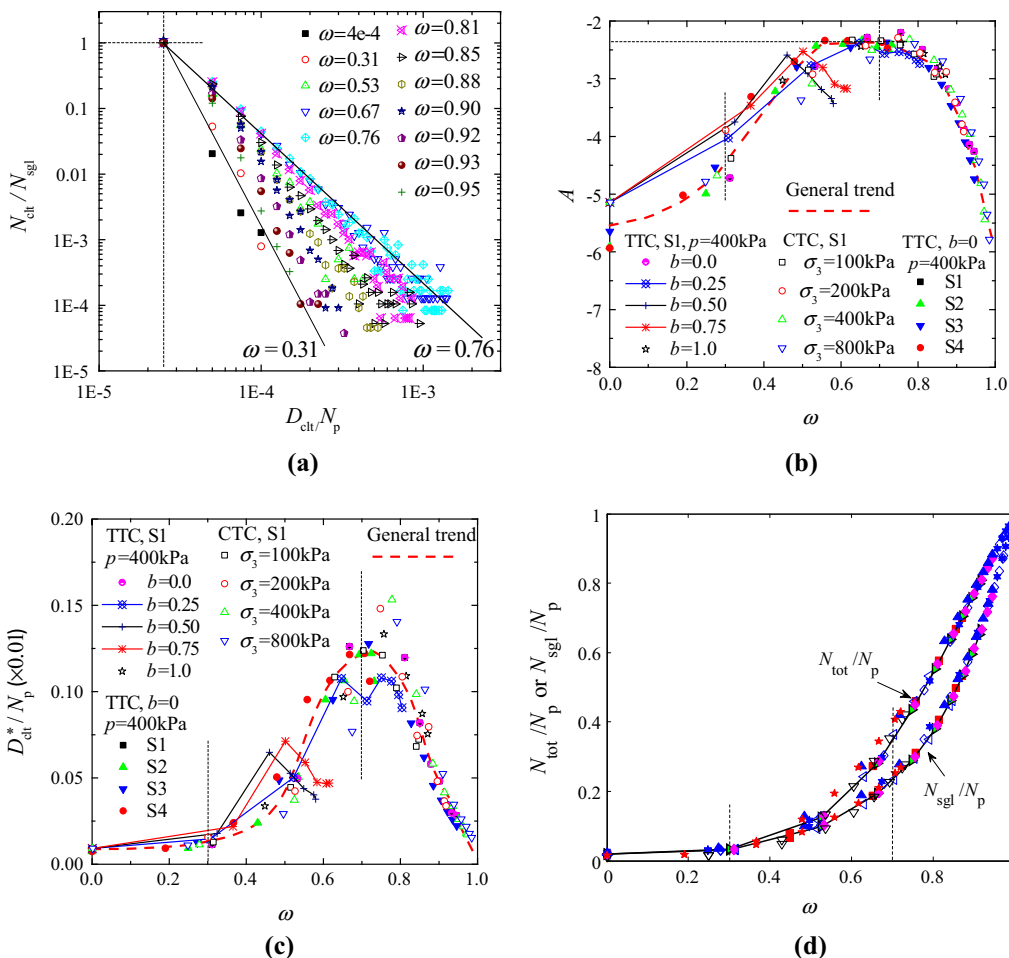


**Fig. 13** Evolutions of **a** cluster size distribution in *effective cluster* group, **b** fitting parameter *A*, **c** threshold cluster size and **d** total and single-particle cluster numbers

### 6 Cluster evolution stages and implications for constitutive modeling

The observations in Figs. 12 and 13 imply that cluster evolution roughly has three distinct stages that can be delimited by bond breakage ratio  $\omega = 0.3$  and  $0.7$ . Figure 14 presents typical variations of threshold cluster size and the size and number of *disperse clusters*. Each hollow triangle represents one *disperse cluster* in the upper plot of Fig. 14.

*Stage I* ( $\omega$  between 0 and 0.3). The initial intact cemented assembly can be viewed as a single cluster, named *mother cluster* (the largest cluster in a sample) hereafter. In this stage, the *Mother cluster* is the only *disperse cluster* and its size ( $D_{clt,max}$ ) only decreases slightly as shown in Fig. 14. In Fig. 13d, the cluster number  $N_{tot}$  and single-particle cluster number  $N_{sgl}$  are very close in this stage, implying that bond breakage mainly leads to detachment of single particles from the *mother cluster*. In this stage, the *mother cluster* acts as a skeleton to bear

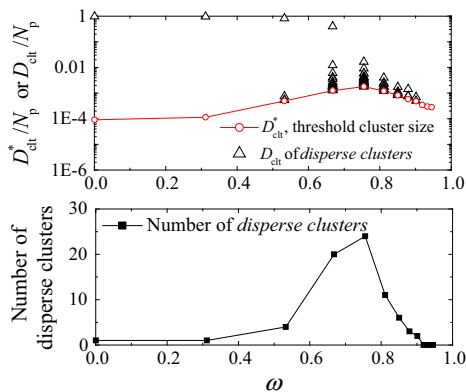


**Fig. 14** Evolutions of *disperse cluster* size and number (sample S1, TTC,  $b = 0.0$ ,  $p = 400$  kPa)

external load, but it is gradually deteriorated due to the ongoing detachment of single particles. To quantitatively examine this feature, the average stress  $\sigma_{ij}$  of a granular assembly is expressed as



$$\begin{aligned} \sigma_{ij} &= \frac{1}{V} \sum_{k=1}^{N_p} \sum_{m=1}^{N_{c,k}} f_j l_i \\ &= \underbrace{\frac{1}{V} \sum_{k=1}^{D_{\text{clt,max}}} \sum_{m=1}^{N_{c,k}} f_j l_i}_{\sigma_{ij,s}} + \underbrace{\frac{1}{V} \sum_{k=1}^{N_p - D_{\text{clt,max}}} \sum_{m=1}^{N_{c,k}} f_j l_i}_{\sigma_{ij,d}} = \sigma_{ij,s} + \sigma_{ij,d} \end{aligned} \tag{15}$$

where  $V$  is the sample volume,  $f_j$  is the contact force,  $l_i$  is a vector pointing from particle centroid to contact center and  $N_{c,k}$  is the number of contacts around particle  $k$ . The stress can be partitioned into two parts, representing stresses in the *mother cluster* skeleton ( $\sigma_{ij,s}$ ) and detached particles  $\sigma_{ij,d}$ , respectively.

Figure 15 presents the contribution of detached particles to the overall stress. The very little contribution of  $\sigma_{i,d}$  (less than 0.5%) indicates that the detached particles actually float in the *mother cluster* skeleton voids. This observation agrees with the assumption in traditional continuum damage mechanics that microcracks behave like voids, i.e., taking no load. (Note that traditional continuum damage mechanics can be viewed as a special case in the binary-mixture-type model framework.) As shown in Fig. 5, at the end of this stage, the structured sand either has just passed the peak state in a softening response or is in the hardening process but with a deviator stress close to the peak. In a geotechnical problem where failure initiation is the major concern and post-failure response is not the issue, traditional continuum damage mechanics framework (or binary-mixture-type model framework with no contribution from the remolded part) is physically proper to describe the behavior of structured sand in this stage.

*Stage II* ( $\omega$  between 0.3 and 0.7). With increasing bond breakage, the *mother cluster* is crushed into pieces, which are then further crushed into smaller clusters, forming a continuously distributed *effective cluster* group as shown in Fig. 13a. This leads to a quick increase in the numbers of total and single-particle clusters and their difference ( $N_{\text{tot}} - N_{\text{sgl}}$ ) in Fig. 13d. The rapid increase in threshold cluster size  $D_{\text{clt}}^*$  and the number of *disperse clusters* in Fig. 14 indicates a growing diversity of cluster size in both

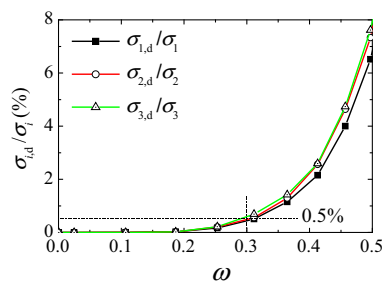


Fig. 15 Contribution of detached particles to the overall stress (sample S1, TTC,  $b = 0.0$ ,  $p = 400$  kPa)

effective and disperse cluster groups. Figure 14 also indicates that the size span in *disperse cluster* group reduces significantly as bonds break. This stage ends up with a spatial cluster configuration shown in Fig. 9 where clusters of various sizes and shapes are interwoven.

In this stage, clusters of all sizes are taking load. A smooth and continuous transition from continuum to granular material is observed in this stage. The binary-mixture-type models treat structured sand as a composite material consisting of structured part and remolded part [12, 14, 47], which is physically consistent with the scenario numerically observed in this stage. Therefore, physical fidelity is well respected if the binary-mixture-type model framework could be adopted to develop a constitutive model of structured sand in this stage.

*Stage III* ( $\omega$  between 0.7 and 1.0). In this stage, the threshold cluster size decreases rapidly, indicating a decaying diversity in particle size, but both  $N_{\text{tot}}$  and  $N_{\text{sgl}}$  increase at the largest rates ever as shown in Fig. 13. Figure 14 shows the decrease in both diversity and number of *disperse cluster* group. Finally, all the bonds are broken and the cemented assembly is totally disturbed.

In this stage, there is no cluster as large as the assembly dimension. The external load is transmitted through contacts within and between clusters. The assembly’s granular feature prevails over its continuum feature. The binary-mixture-type framework is physically reliable as explained above. Besides, the assembly can be viewed as a special clean sand with crushable particles (clusters being regarded as particles). Therefore, crushable sand models [45, 46] may be borrowed for constitutive description of the heavily disturbed structured sand in this stage.

In summary, the elasto-plastic soil models must be highly phenomenological for cemented granular material due to its highly conceptualized yielding, plastic flow and hardening/softening that cannot reflect the mesoscale cluster behavior. Micromechanics-based model should somehow consider the cluster evolution in its derivation from contact behavior to macroscopic behavior to achieve physical fidelity. The binary-mixture-type model framework is the closest to the numerically observed physical scenario among the three categories of constitutive models. The focus would be put on partitioning the cemented granular assembly into two parts in the binary-mixture-type model framework, and one promising solution is inter-cluster contacts being one part and intra-cluster contacts being the other part.

## 7 Conclusions

This study focuses on the formation and evolution of bonded particle clusters, a salient mesoscale feature of cemented granular material, such as structured sand in

geomechanics. DEM simulation results on structured sand show that the macroscopic stress–strain behavior and bond breakage rate are influenced by stress conditions, sample density and bond content. The heterogeneous nature of granular material leads to highly non-uniform deformation at local cell level. The large cell-level deformation rate is a consequence of bond breakage.

Bonded particle clusters are angular in shape and have various sizes. Clusters with different sizes and shapes are interwoven in microstructure. Statistically, smaller clusters are less angular in shape and have less weak points.

The externally applied stress/strain drives the evolutions of cluster size, number and angularity. DEM simulation results suggest three stages in the cluster formation and crushing process. In stage I (bond breakage ratio  $\omega$  between 0 and 0.3), single particles are spatially randomly detached from the initial intact assembly (*mother cluster*); the *mother cluster* bears external load while the detached single particles mainly float in the voids. In stage II ( $\omega$  between 0.3 and 0.7), a family of clusters with growing size diversity are formed; the cluster size and cluster number follow a linear relationship in a double-logarithmic plot. In stage III ( $\omega$  between 0.7 and 1.0), the cluster size diversity drops quickly, and finally, all clusters are crushed into single particles.

The purpose of this paper is not to establish a specific constitutive model for cemented granular material. Instead, the applicability and future development of three constitutive model frameworks for cemented granular material are discussed based on the numerical simulation results. From the view of physical fidelity, the binary-mixture-type model framework is very promising to capture the complete mesoscale structure evolution of cemented granular material.

Experimental verification of the simulated cluster evolution is greatly desired in future work. This study focuses on cluster evolution at a sample scale. How clusters form and evolve at field scale and whether sample scale observations are alike field-scale observations deserve further study.

**Acknowledgements** The research is funded by China Postdoctoral Science Foundation with Grant No. 2018M642233, Postdoctoral Science Foundation of Jiangsu Province with Grant No. 2018K135C, Foundation for Research Initiation at Nanjing Tech University with Grant No. 3827401759 and National Natural Science Foundation of China with Grant Nos. 51678300 and 51639008 (key program), which are sincerely appreciated.

## References

- Airey DW (1993) Triaxial testing of naturally cemented carbonate soil. *J Geotech Eng (ASCE)* 119(9):1379–1398
- Bagi K (1996) Stress and strain in granular assemblies. *Mech Mater* 22(3):165–177
- Bono JP, McDowell GR (2013) Discrete element modelling of one-dimensional compression of cemented sand. *Granul Matter* 16(1):79–90
- Brendel L, Torok J, Kirsch R, Brockel U (2011) A contact model for the yielding of caked granular materials. *Granul Matter* 13(6):777–786
- Brown NJ, Chen J-F, Ooi JY (2014) A bond model for DEM simulation of cementitious materials and deformable structures. *Granul Matter* 16(3):299–311
- Ciantia MO, Castellanza R, Crosta GB, Hueckel T (2015) Effects of mineral suspension and dissolution on strength and compressibility of soft carbonate rocks. *Eng Geol* 184:1–18
- Collins BD, Sitar N (2011) Stability of steep slopes in cemented sands. *J Geotech Geoenviron Eng* 137(1):43–51
- Consoli NC, Vendrusco MRA, Prietto PDM (2003) Behavior of plate load tests on soil layers improved with cement and fiber. *J Geotech Geoenviron Eng* 129(1):96–101
- Cuccovillo T, Coop M (1997) Yielding and pre-failure deformation of structured sands. *Géotechnique* 47(3):491–508
- Cuccovillo T, Coop M (1999) On the mechanics of structured sands. *Géotechnique* 49(6):741–760
- Delenne JY, El Youssoufi MS, Cherblanc F, Benet JC (2004) Mechanical behaviour and failure of cohesive granular materials. *Int J Numer Anal Met Geomech* 28(15):1577–1594
- Desai CS, Toth J (1996) Disturbed state constitutive modeling based on stress-strain and nondestructive behavior. *Int J Solids Struct* 33(11):1619–1650
- Ebinuma T, Kamata Y, Minagawa H, Ohmura R, Nagao J, Narita H (2005) Mechanical properties of sandy sediment containing methane hydrate. In: *Proceeding of 5th international conference on gas hydrates*, pp 958–961
- Haeri SM, Hamidi A (2009) Constitutive modelling of cemented gravelly sands. *Geomech Geoeng* 4(2):123–139
- Hicher PY, Chang CS, Dano C (2008) Multi-scale modeling of grouted sand behavior. *Int J Solids Struct* 45(16):4362–4374
- Hyodo M, Yoneda J, Yoshimoto N, Nakata Y (2013) Mechanical and dissociation properties of methane hydrate-bearing sand in deep seabed. *Soils Found* 53(2):299–314
- Ismail MA, Joer HA, Randolph MF, Meritt A (2002) Cementation of porous materials using calcite. *Géotechnique* 52(5):313–324
- Itasca Consulting Group (2008) PFC3D (particle flow code in three dimensions) user's guide. Minneapolis
- Jiang MJ, Leroueil S, Konrad JM (2005) Yielding of microstructured geomaterial by distinct element method analysis. *J Eng Mech-ASCE* 131(11):1209–1213
- Jiang MJ, Yu HS, Harris D (2006) Bond rolling resistance and its effect on yielding of bonded granulates by DEM analyses. *Int J Numer Anal Met Geomech* 30(8):723–761
- Jiang MJ, Liu F, Zhou YP (2014) A bond failure criterion for DEM simulations of cemented geomaterials considering variable bond thickness. *Int J Numer Anal Met Geomech* 38(18):1871–1897
- Jiang MJ, Jin SL, Shen ZF, Liu W, Coop MR (2015) Preliminary experimental study on three-dimensional contact behavior of bonded granules. In: *IOP conference series: earth and environmental science*. IOP Publishing, vol. 26, no. 1, pp 12007–12014
- Jiang MJ, Shen ZF, Wang JF (2015) A novel three-dimensional contact model for granulates incorporating rolling and twisting resistances. *Comput Geotech* 65:147–163
- Jiang M, Liu W, Liao Z (2017) A novel rock contact model considering water-softening and chemical weathering effects. In: *Proceedings of the 7th international conference on discrete element methods*. Springer, Singapore, pp 455–463

25. Kirsch R, Bröckel U, Brendel L, Török J (2011) Measuring tensile, shear and torsional strength of solid bridges between particles in the millimeter regime. *Granul Matter* 13(5):517–523
26. Kuhn MR (1997) Deformation measures for granular materials. In: Chang CS, Misra A, Liang RY, Babic M (eds) *Mechanics of deformations and flow of particulate materials*. ASCE, New York, pp 91–104
27. Lagioia R, Nova R (1995) An experimental and theoretical study of the behavior of a calcarenite in triaxial compression. *Géotechnique* 45(4):633–648
28. Leroueil S, Vaughan PR (1990) The general and congruent effects of structure in natural soils and weak rocks. *Géotechnique* 40:467–488
29. Lo SR, Wardani SP (2002) Strength and dilatancy of a silt stabilized by a cement and fly ash mixture. *Can Geotech J* 39(1):77–89
30. Masui A, Haneda H, Ogata Y, Aoki K (2005) Effects of methane hydrate formation on shear strength of synthetic methane hydrate sediments. In: *Proceedings of the 5th international offshore and polar engineering conference*, pp 364–369
31. Miyazaki K, Masui A, Sakamoto Y, Aoki K, Tenma N, Yamaguchi T (2011) Triaxial compressive properties of artificial methane-hydrate-bearing sediment. *J Geophys Res* 116(B6). <https://doi.org/10.1029/2010JB008049>
32. Nicot F, Darve F (2005) A multiscale approach to granular materials. *Mech Mater* 37(9):980–1006
33. Nicot F, Darve F (2011) The H-microdirectional model: accounting for a mesoscopic scale. *Mech Mater* 43(12):918–929
34. Nova R, Castellanza R, Tamagnini C (2003) A constitutive model for bonded geomaterials subject to mechanical and or chemical degradation. *Int J Numer Anal Met Geomech* 27(9):705–732
35. Obermayr M, Dressler K, Vrettos C, Eberhard P (2013) A bonded-particle model for cemented sand. *Comput Geotech* 49:299–313
36. Pinkert S, Grozic JL (2015) Failure mechanisms in cemented hydrate-bearing sands. *J Chem Eng Data* 60(2):376–382
37. Potyondy DO, Cundall PA (2004) A bonded-particle model for rock. *Int J Rock Mech Min* 41(8):1329–1364
38. Shen ZF, Jiang MJ (2016) DEM simulation of bonded granular material. Part II: extension to grain-coating type methane hydrate bearing sand. *Comput Geotech* 75:225–243
39. Shen ZF, Jiang MJ, Wan R (2016) Numerical study of inter-particle bond failure by 3D discrete element method. *Int J Numer Anal Met Geomech* 40:523–545
40. Shen ZF, Jiang MJ, Thornton C (2016) DEM simulation of bonded granular material. Part I: contact model and application to cemented sand. *Comput Geotech* 75:192–209
41. Wang YC, Alonso-Marroquin F (2009) A finite deformation method for discrete modeling: particle rotation and parameter calibration. *Granul Matter* 11(5):331–343
42. Wang YH, Leung SC (2008) A particulate-scale investigation of cemented sand behavior. *Can Geotech J* 45(1):29–44
43. Wang YH, Leung SC (2008) Characterization of cemented sand by experimental and numerical investigations. *J Geotech Geoenviron Eng* 134(7):992–1004
44. Wang H, Gong H, Liu F, Jiang MJ (2017) Size-dependent mechanical behavior of an intergranular bond revealed by an analytical model. *Comput Geotech* 89:153–167
45. Xiao Y, Liu H, Ding X, Chen Y, Jiang J, Zhang W (2016) Influence of particle breakage on critical state line of rockfill material. *Int J Geomech* 16(1). [https://doi.org/10.1061/\(ASCE\)GM.1943-5622.0000538](https://doi.org/10.1061/(ASCE)GM.1943-5622.0000538)
46. Xiao Y, Liu H, Chen Q, Ma Q, Xiang Y, Zheng Y (2017) Particle breakage and deformation of carbonate sands with wide range of densities during compression loading process. *Acta Geotech* 12(5):1177–1184
47. Yu YZ, Pu JL, Ugai K (1998) A damage model for soil-cement mixture. *Soils Found* 38(3):1–12

**Publisher's Note** Springer Nature remains neutral with regard to jurisdictional claims in published maps and institutional affiliations.